JOURNAL OF APPLIED PHYSICS **104**, 013303 (2008)

# Experimental investigation of ultraviolet laser induced plasma density and temperature evolution in air

Magesh Thiyagarajan[a] and John Scharer
*Electrical and Computer Engineering Department, University of Wisconsin, Madison, Wisconsin 53706, USA*

(Received 22 December 2007; accepted 3 May 2008; published online 11 July 2008)

We present measurements and analysis of laser induced plasma neutral densities and temperatures in dry air by focusing 200 mJ, 10 MW high power, 193 nm ultraviolet ArF (argon fluoride) laser radiation to a 30 $\mu$m radius spot size. We examine these properties that result from multiphoton and collisional cascade processes for pressures ranging from 40 Torr to 5 atm. A laser shadowgraphy diagnostic technique is used to obtain the plasma electron temperature just after the shock front and this is compared with optical emission spectroscopic measurements of nitrogen rotational and vibrational temperatures. Two-color laser interferometry is employed to measure time resolved spatial electron and neutral density decay in initial local thermodynamic equilibrium (LTE) and non-LTE conditions. The radiating species and thermodynamic characteristics of the plasma are analyzed by means of optical emission spectroscopy (OES) supported by SPECAIR, a special OES program for air constituent plasmas. Core plasma rotational and vibrational temperatures are obtained from the emission spectra from the $N_2C$-$B(2+)$ transitions by matching the experimental spectrum results with the SPECAIR simulation results and the results are compared with the electron temperature just behind the shock wave. The plasma density decay measurements are compared with a simplified electron density decay model that illustrates the dominant three-and two-body recombination terms with good correlation. 
[DOI: 10.1063/1.2952540]

## I. INTRODUCTION

Due to continued development of lasers with high powers and shorter wavelengths, there has been steady interest in laser induced breakdown plasmas. Emphasis in more recent years has been on short-wavelength excimer lasers such as 0.35 $\mu$m (XeF) and 0.25 $\mu$m (KrF).[1] Strickler[2] measured the air breakdown threshold at 1.06 $\mu$m and compared it to the microwave case. However, no research has been carried out to date on plasma formation measurements for air using an ultraviolet excimer laser radiation at 193 nm (ArF). 193 nm UV excimer laser radiation has been widely used in industrial applications especially in semiconductor processing and micromachining and also in high voltage laser triggering and switching applications.[3] This research examines the air plasma densities and temperatures formed by a shorter wavelength laser than have been examined previously where quantum multiphoton processes play a significant role.

The energy deposition into a gas by a focused laser beam can be described by four progressive steps: (1) initial release of electrons by the multiphoton effect,[4] (2) ionization of the gas in the focal region by the collisional cascade ionization producing electrons, (3) absorption and partial reflection and scattering of laser energy by the gaseous plasma, and (4) formation and propagation of a detonation shock wave into the surrounding gas and relaxation of the focal region plasma. In addition, other investigators[4–7] operating at longer wavelengths have observed a residual vortex ring formed by the asymmetric plasma formation in quiescent air.

The characteristics of the laser induced plasma are diagnosed by several optical diagnostics. The laser energy absorbed by the plasma and the laser energy transmitted through the plasma are measured using a laser energy detector. We have also applied the plasma shadowgraphy technique[7] using a fast gating imaging technique for visualizing the gas-dynamic processes of the laser induced plasma. Shadowgraphy measurements in and near the focus can shed light on postbreakdown effects. Using this technique one can measure the velocity of plasma expansion and the laser heated neutral density shock wave immediately after the breakdown. The electron temperature just behind the neutral shock wave created by the $>1\ \mathrm{TW/cm^2}$ focused laser is measured by determination of the expansion velocities, using Zeldovich and Raizer's[8] tabulated flow quantities. The electron temperature just behind the shock wave front in air with standard conditions just ahead of the wave ($p_0=1$ atm and $T_0=293$ K) is determined. High resolution, two-color laser interferometry[7,9] is developed to measure both temporal and spatial electron and neutral densities. The plasma decay measurements are compared with a simplified model based on the continuity equation to analyze the dominant loss mechanisms involved in the plasma decay such as two- and three-body recombination losses. Optical emission spectroscopy (OES) is carried out to diagnose the nitrogen radiating species and thermodynamic characteristics of the laser induced core plasma. The existence of characteristic bands in the spectra obtained from the nitrogen plasma emission signifies the presence of certain excited states of the molecular species in the plasma. The rotational and vibrational temperatures of

[a]Electronic addresses: thiyagar@ge.com and thiyagarajan@wisc.edu.

 

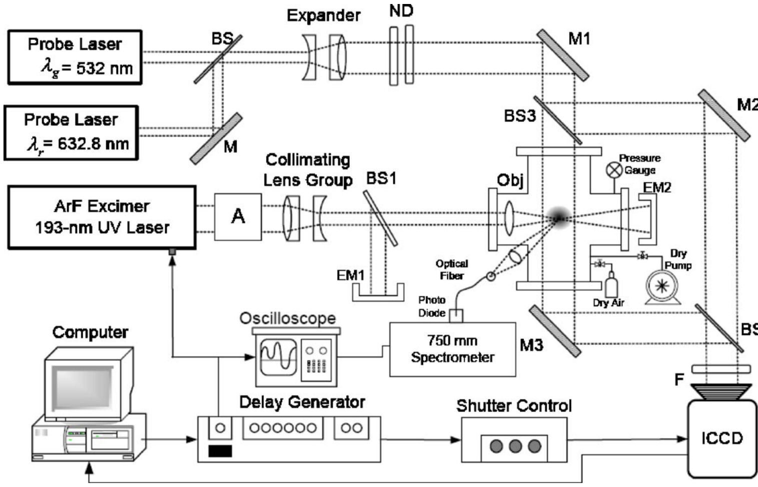


FIG. 1. (Color online) Schematic of the experimental and diagnostic setup of 193 nm laser induced plasma. (A) Attenuator, (BS) beam splitter, (EM) energy meter, (Obj) objective lens, (M) mirror, (F) filter, and (ND) neutral density filter.

the nitrogen species in the laser induced plasma can be obtained by analyzing the profiles and the emission intensity ratios of the associated species. The experimentally observed $N_2C$-$B(2+)$ spectrum results are analyzed and compared with the code-simulated results from SPECAIR,[10] an OES simulation program for air constituent plasmas. These core temperatures are compared with the electron temperature during the shock wave plasma expansion. The experimental system and diagnostics are presented in Sec. II, experimental results are discussed in Sec. III, and a summary is presented in Sec. IV.

## II. EXPERIMENT

### A. Excimer laser induced plasma system

The schematic diagram of the experimental setup is shown in Fig. 1. In this experiment, a pulsed 193 nm excimer laser (Lumonics, Pulsemaster PM-842, argon fluoride, $\lambda = 193$ nm, 6.4 eV per photon) that runs with a gas mixture containing 5% $F_2$ in He was operated shot by shot. The laser output is a rectangular beam with cross section of $2.8 \times 1.2$ cm$^2$ with homogeneous ($\pm 5\%$) beam intensity. The full width at half maximum (FWHM) of the laser pulse is $20 \pm 2$ ns, with a 2 ns rise/fall time and a maximum available laser output energy of 200 mJ. A typical working output of up to $180 \pm 5$ mJ is used in the experiment.

The rectangular cross section of the laser beam was reduced to $1 \times 1$ cm$^2$ using a set of 193 nm matched coated cylindrical Suprasil plano-convex and cylindrical plano-concave ($f = 10$ cm and $d = 5$ cm) UV fused silica lenses to more closely match the 1 cm diameter objective focus lens. In this experiment, all UV optical components are specially coated, with 98% transmission at 193 nm. The laser energy passing through the cylindrical lenses is measured using a laser energy meter (Scientech, AC 50 UV Calorimeter and Astral, AD30 Laser Energy Meter).

The laser beam enters the plasma chamber through a 193 nm transmission coated 3 cm diameter Suprasil UV quartz window. The laser beam was focused by using a high power handling (100 MW/cm$^2$) objective lens mounted inside the plasma chamber. The objective lens (OFR, LMU-10X-193) has an effective focal length of 20 mm, with a 10 mm entrance aperture and a 0.25 numerical aperture. Due to its short focal length the objective lens is mounted inside the plasma chamber using an adjustable length holder so that the laser induced plasma is positioned on the cylindrical chamber axis. Space between the entrance UV window and the objective lens is maintained at the same pressure as that of the chamber pressure in order to avoid differential pressures acting on the objective lens. Great care was taken to position the objective lens together with the plasma chamber precisely in the line of sight with the UV laser beam for the air breakdown experiments.

Following the $1 \times 1$ cm$^2$ reduced size laser beam from the plano-concave lens, the objective focus lens uses only the center 1 cm diameter circular portion and the excess portion around the edges of the beam is eliminated. By eliminating the edges of the laser beam, edge effects that could affect the focus of the uniform laser beam are minimized. Utilizing this technique, 21% of the laser output beam energy is measured to be lost. In addition, measurements show that the laser beam experiences a 6% loss as it passes through the coated UV optics including the cylindrical plano-convex/concave lenses, a Suprasil UV quartz window, and the objective focal lens. These results are obtained using a laser energy meter (Scientech, AC 50 UV Calorimeter and Astral, AD30 Laser Energy Meter). The laser energy available immediately after the objective lens corresponding to a $180 \pm 5$ mJ laser output was measured by the Scientech energy meter to be $135 \pm 5$ mJ, corresponding to the measured incident laser energy on the focal spot.

The plasma chamber was made from stainless steel and was designed to hold pressures from 10 mTorr to 6 atm (4560 Torr). Optical view ports on both sides of the cell are made of 3 cm diameter, 5 mm thick sapphire windows to withstand pressures up to 6 atm. The view ports enabled observation of the interior at right angles to the cell axis that is coincident with the direction of the laser beam, as well as for diagnosing the plasma. The chamber was evacuated with a dry scroll pump (Varian, SH-110) down to 10 mTorr and flushed several times before finally filling with dry air ($<10$ ppm water) to the desired pressure. The chamber pressure was measured precisely by two pressure gauges, a MicroPirani vacuum gauge with a pressure controller readout

(MKS Instruments, 910–11 and PDR 900–11) to measure pressure ranges from 10 to 1500 Torr and a high pressure digital pressure gauge (GE, Druck DPI 104) capable of measuring pressure ranges from 760 Torr to 10 atm. The gas flow through the chamber was regulated by a needle valve in the gas line and another valve in the pumping line. For one set of experiments to determine the effects of removing microdust particles of diameter $\geq 0.1$ $\mu$m on the breakdown threshold of dry air, we have inserted a filter capsule in the incoming gas line and cleaned residual dust on window and lens surfaces by means of an aerosol jet. The filter houses a dual-pleated polytetrafluoroethylene filtering element with $\leq 0.1$ $\mu$m pore size.

### B. Shadowgraphy diagnostics

In a plasma, the refractive index is primarily a function of the electron density, which is the main plasma parameter determined by refractive index measurements. Typical plasma diagnostics based on refractive effects include interferometry, Schlieren imaging, shadowgraphy, and Faraday rotation measurements.[7] While the interferometry technique gives a direct measure of the refractive index $\mu$, the Schlieren and the shadowgraphy techniques probe the refractive index gradient, $d\mu/dx$. In this experiment the shadowgraphy technique is applied for visualizing the laser induced plasma and laser heated gas dynamic processes. In general, a shadowgraph is a measure of the refraction of light rays as they pass through a medium. An electromagnetic wave exerts a force on the charged constituents of the medium through which it propagates. This force accelerates the charges that in turn modify the time-varying electromagnetic field. A solution of electromagnetic wave propagation in a plasma can be obtained by solving the wave equation for a plane wave in the small amplitude approximation.[11] The plasma-refractive index then follows as

$$\mu = \left(1 - \frac{\omega_p^2}{\omega^2(1 \pm \omega_e/\omega)[1 - i(v/w)]}\right)^{1/2}, \tag{1}$$

where $\omega = 2\pi c/\lambda$ is the frequency of the electromagnetic wave. In our case $\lambda = 532$ nm and no dc magnetic field ($\omega_e = 0$). The electron plasma frequency is $\omega_p = (n_e e^2/\varepsilon_0 m_e)^{1/2}$ and $\nu$ is the effective number of collisions per second that an electron makes with neutrals.

In our case $v/\omega \ll 1$, the collision rate in atmospheric (760 Torr) air plasma is of the order of $10^{11}$ Hz (Ref. 12) and negligible compared to $\omega$ and therefore Eq. (1) simplifies to

$$\mu_{\text{electrons}} = \sqrt{1 - \frac{\omega_p^2}{\omega^2}} = \sqrt{1 - \frac{n_e}{n_e}}, \tag{2}$$

where

$$n_c = \frac{4\pi^2 c^2 \varepsilon_0 m_e}{e^2 \lambda^2} = \frac{\pi}{r_e \lambda^2} \tag{3}$$

is the cutoff density and $r_e = e^2/(4\pi\varepsilon_0 m_e c^2) = 2.818 \times 10^{-15}$ m is the classical electron radius. In our shadowgraphy experiments, as shown in Fig. 1, a green laser at $\lambda = 532$ nm is used as a light source due to its coherence, brightness, and narrow bandwidth. The cutoff density for 532 nm is $3.9 \times 10^{21}$ cm$^{-3}$, which is well above the densities encountered in our laser focused plasma experiments.

### C. Two-color laser interferometry diagnostics

High resolution two-color laser interferometry diagnostics[7,9] were realized using two different wavelengths to simultaneously measure the electron density ($n_e$) and neutral gas density ($n_0$) of the laser induced plasma as well as the neutral gas density of the laser heated gas with spatial and temporal evolution. The diagnostic arrangement is shown in Fig. 1. The interferometer works in the Mach–Zehnder configuration, in which the plasma is located in one of the arms of a two beam interferometer. The interferometer is configured to acquire an interference image of adjacent fringes of equal width when no plasma is formed. The changes in the optical index of the environment due to the presence of plasma and neutral gas profiles create a shift in the fringes that corresponds to the electron and neutral density profiles in the line of sight. These fringing patterns are captured by an intensified charged-coupled device (ICCD) (ANDOR, DH 734) of $1024 \times 1024$ active pixels and a $30 \times 30$ $\mu$m$^2$ resolution camera with a minimum gate width of 10 ns connected to a computer.

The plasma is illuminated by two 1 mm diameter probe lasers, a He–Ne red laser emitting at $\lambda_R = 632.8$ nm (JDS Uniphase 1125P), and a high performance solid state green laser emitting at $\lambda_G = 532$ nm (Edmund Optics, NT56–484) operated independently at 5 mW power levels. The probe laser beam sizes are expanded by a factor of 20 using an optical beam expander (Edmund Optics, NT55–579) and a 20 mm aperture eliminates the edges of the expanded beam to improve the beam quality. The Gaussian wave front is split by a 50/50 beam splitter with one beam sent through the plasma chamber and the other used as a reference beam. Since the coherence length of the probe laser determined by the probe laser bandwidth of 0.05 nm is only 5.7 mm, both arms of the interferometer were adjusted to the same optical length of 61 cm within a few mm ($<5$ mm) offset. A mismatch of the two wave fronts by one coherence length causes a drop of the fringe contrast by a factor of $1/e$. The two view port windows on either side of the chamber are slightly tilted relative to the probe beam laser beam axis to avoid ghost images due to reflections. Optical interference filters with center wavelength at $532 \pm 2$ or $632.8 \pm 2$ nm are used in front of the ICCD to suppress the plasma self-luminescence.

Both the test and the reference beams are aligned to overlap within 200 $\mu$m to assure the desired spatial resolution. The mirror for the reference beam is slightly tilted relative to the laser beam axis using a micropositioner. In this way a fringe pattern with the number of fringes proportional to the tilting angle is observed. A tilting of the mirror in the other plane rotates the fringe pattern. In the measurements, the null fringe pattern was arranged to show between eight and ten fringes over the 1.3 cm width field of view perpendicular to the observation axis.

By using a digital delay generator the gating trigger pulse of the ICCD is precisely synchronized with the firing pulse of the excimer UV laser. These two pulses are compared by means of a 1 GHz sample rate oscilloscope (LeCroy, WaveRunner 6100A). The gate width of the ICCD is varied by using an electronic shutter controller with a typical gate width of 10 ns. Due to the high sensitivity of the ICCD, the milliwatt level cw powers of from the red and green lasers are sufficient to record images with a gate width of 10 ns.

### D. OES

The OES diagnostic setup is used as shown in Fig. 1 to measure the rotational ($T_{rot}$) and vibrational ($T_{vib}$) temperatures of the laser induced plasma. A high resolution narrow band (0.01 nm resolution) monochromator (Acton Research, model ARC-SP-2758) is used. The monochromator has a multiple grating option, which gives the flexibility of choosing the resolution and wavelength range. A holographic grating of $68\times 68$ mm, 2400 grooves/mm, optimized for the entire visible wavelength range is used to acquire emission spectrum. The plasma emission is acquired by a collecting lens ($f/10$) and sent to a fast gating Andor iStar ICCD (ANDOR, DH 734) through a high-quality (200–800 nm) fiber-optic bundle. The Andor iStar ICCD detector is integrated with an Acton SpectraPro 2750 spectrograph system. This system has a near-Lorentzian slit function with a half-maximum width of 0.2 nm when the grating density is set to 1200 lines/mm. The UV excimer laser is synchronized with the gated ICCD in such a way that the spectral emissions from the laser induced plasma are acquired at different plasma lifetimes ranging from 45 ns to 100 $\mu$s with a gating time of $t_g=45$ ns for time windows $t<100$ ns and $t_g=100$ ns for time windows $t>100$ ns. The spectral emission signal strength of the laser induced plasma spark is very weak due to small plasma dimension and short gating times of 45–100 ns. In order to obtain good signal strength and spectral profile, 2000 laser shots are used at each acquisition time and the laser is operated at 1 Hz to maintain the same laser energy output.

The initial laser induced plasmas are generally observed to be in local thermodynamic equilibrium (LTE) since these laser induced plasmas are at high densities ($10^{15}-10^{18}$ cm$^{-3}$).[12,13] For plasmas in LTE, a single temperature characterizes all internal energy modes (translational, vibrational, and rotational). The rotational ($T_{rot}$) and vibrational ($T_{vib}$) temperatures can be measured from the $N_2 C$-$B(2+)$ ($N_2$ second positive band system) rotational and vibrational transitions[13] by matching them with the code-simulated results from SPECAIR.[10] SPECAIR is a computer simulation software developed by Laux *et al.*[12–14] on the basis of the nonequilibrium air radiation code (NEQAIR) by Park.[15] SPECAIR performs the OES by determining the populations of the states of the radiative transitions using user-specified electronic, vibrational, and rotational temperatures.[14,16–18] The modeled transition rates are calculated based on tabulated data for the transitions. From the calculated transition probabilities and populations of radiating species, the line-by-line optical emission intensity is computed for the wavelengths of the transitions.[13,14,16] SPECAIR is quite suitable for LTE plasma optical emission studies, making it an ideal software tool for our analysis of the high density laser induced air constituent plasmas. These OES results are compared with the electron temperature associated with the propagating neutral density shock wave.

## III. EXPERIMENTAL MEASUREMENTS, RESULTS, AND DISCUSSION

### A. Excimer laser: Output, incident, transmitted, and absorbed energies

As noted earlier, the 193 nm excimer laser has a maximum output of 200 mJ, $20\pm 2$ ns FWHM pulse with a 2 ns rise/fall time. A stable working output energy of $180\pm 5$ mJ is maintained throughout the experiment. While removing the edges of the square laser beam, 21% of the laser energy is lost and there is a 6% loss of the laser output energy while passing through the UV focusing optics. The losses were determined by placing the individual UV optics in the laser beam path and the transmitted energy was measured using the Astral energy meter.

With the UV focusing optics in place, a laser energy of $135\pm 5$ mJ was measured immediately after the objective lens by placing the laser energy detector surface in contact with the output edge of the objective lens where the laser intensity is not sufficiently high to damage the detector. Therefore, a laser energy of $135\pm 5$ mJ was incident and focused onto the 30 $\mu$m radius spot size. This transmitted energy level is used as a reference level for all additional measurements in this research.

A luminous plasma was observed for all 180 mJ laser pulses at the focal spot, 20 mm from the edge of the objective lens. In order to measure the transmitted energy through the plasma, the 5 cm diameter sensor energy meter was placed 20 mm after the focal spot, where the transmitted laser energy can be measured. Since the maximum plasma frequency divided by the laser frequency near the focal spot is $\omega_p/\omega<0.01$, we assume that a very small fraction of the incident laser flux is scattered by the plasma and the laser absorption is primarily due to collisional cascade and multiphoton ionization processes.[31] An average transmitted energy of $80\pm 5$ mJ was measured, which is 60% of the incident energy. Therefore approximately 55 mJ (40% of incident energy) of the excimer laser pulse energy was absorbed at 760 Torr by the plasma at the focal region. The energies absorbed by the plasma at different pressures such as 500 Torr, 3 atm, and 5 atm are measured to be 48, 64, and 76 mJ, respectively, which correspond to 35%, 47%, and 56% of the incident energy, as expected with the increased absorption efficiency with pressure.

### B. Plasma spatial and temporal evolution

In order to understand the dynamical process of the laser induced plasma and the time resolved spatial distribution of the plasma and laser heated neutral gas densities, we developed a laser shadowgraphy diagnostic technique.[7] In the plasma shadowgraphy technique, a synchronized cw probe laser beam is sent through the test section where plasma is located and its image falls directly onto the ICCD with a 1:1 ratio on the image plane. If the refractive index in the test

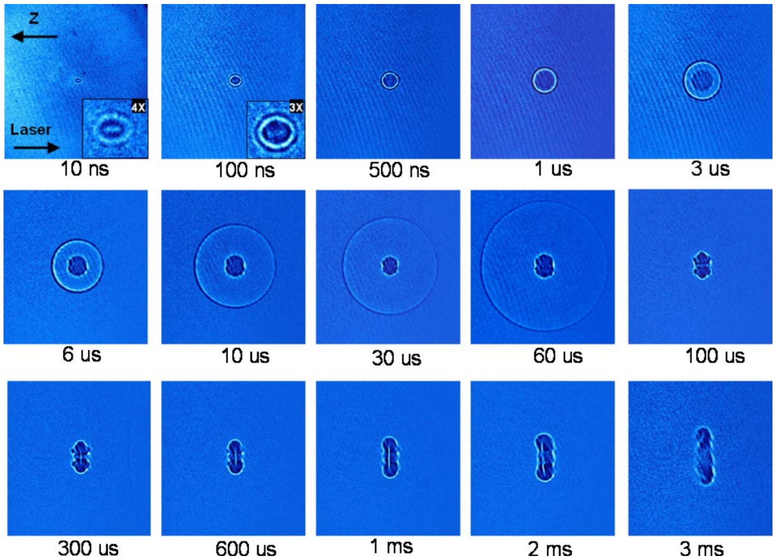


FIG. 2. (Color online) Shadowgrams of the 193 nm laser focused plasma in air, with laser input radiation of 135 mJ energy. Each image has a spatial extent of 1.3 cm. Gating time for each image is 10 ns.

section $\mu$ is uniform, the screen will be essentially uniformly illuminated. If, however, the gradient of $\mu$ varies in space, as one may expect for high density ($10^{14}-10^{18}$ cm$^{-3}$) plasmas, i.e., when there is a significant second derivative of the refractive index, there will be variations in the illumination at the imaging screen. Regions where the second derivative of the refractive index is negative will act like a converging lens.

A comprehensive series of 15 shadowgrams is shown in Fig. 2, in which each image has a spatial extent of 1.3 $\times 1.3$ cm$^2$. These shadowgrams show the spatial and temporal evolution of the laser induced plasma obtained to measure the plasma volume, shockwave velocities, and hot core air pressure. Observation was carried out in the horizontal direction, perpendicular to the axis of UV laser beam that is incident from the left. In Fig. 2 the laser beam propagated in the breakdown section toward the right along the $z$-axis. Positive $z$ is measured from the focal spot in the laser direction. Shadowgrams were obtained in the time span of a few nanoseconds to milliseconds. Time zero was defined at the beginning of the laser pulse. Based on the shadowgraphy images we observe that the plasmas produced for different laser shots are highly reproducible with variations less than 5% due to the laser energy fluctuations. A high bremsstrahlung emission was observed right after breakdown ($t<25$ ns). For good shadowgram definition at $t=10$ ns, the Bremsstrahlung emission captured at a slight earlier time ($t=7$ ns) is subtracted. To achieve high contrast images for 50 ns$<t$ $<100$ $\mu$s, we have integrated 20 shots of the plasma produced during the expansion stage. For $t>100$ $\mu$s single shot images were recorded when the plasma becomes turbulent.

At very early times $t\leq 100$ ns, expansion of the heated region occurs, as a result of which the plasma takes on an asymmetrical shape along the $z$-axis with a clearly expressed sharper tip in the positive $z$ direction. Here time zero ($t=0$) is considered to be the beginning of the laser pulse. After a certain time delay, the plasma reaches an electron density threshold such that the medium substantially absorbs the laser beam and it expands out of the focal volume through a shock wave mechanism.[19] At times up to 600 ns the expanding plasma maintains a spherical shape with a slight oblateness in the $z$ direction. At $\sim 1$ $\mu$s the neutral density shock wave separates from the hot plasma core plasma due to gas heating with a more symmetrical spherical shape and continues to expand as clearly observed in the shadowgrams. Several wave propagation processes have been proposed to explain the plasma expansion phenomenon.[5,19] It should be noted that each image is normalized by its maximum intensity value to preserve detail as the plasma and neutral density decay over time. The expanding shock wave is observed for times up to 60 $\mu$s. Later, the shock wave leaves the 1.3 $\times 1.3$ cm$^2$ field of view followed by a sharp deformation of the irradiated region. It shows that the neutral density shockwave plays an important role for the stability of the hot core plasma expansion by enclosing it as a pressure barrier. The colder air around the focal point region penetrates the hot core air in the focal region, primarily in the $z$ direction. It causes the hot core air to expand and cool. The expansion causes the deformation of the hot core air into a structure of a vortex-type ring up to 2 ms; thereafter the images available lose clarity.

### C. Electron temperature measurements

The shadowgraph images were used to measure the position and expansion velocity of the plasma and gas shock front. The position of the shock wave is measured from the focal point of the focusing lens group. Figure 3 shows the radial position of the shock front as well as the velocity of the plasma and gas shock as a function of time traveling toward the focusing optics, with an absorbed laser energy of 55 mJ at 760 Torr. Based on the measurements and the numerical derivative of the measured position, the curve yields average velocities of 47 km/s, close to the values observed in longer wavelength laser plasma experiments.[7] Zeldovich and Raizer[8] tabulated the flow quantities, primarily the temperature just behind a shock wave front in air with standard conditions ahead of the wave ($p_0=1$ atm and $T_0=293$ K). Figure 4 shows the temperature decay based on the measured velocities of the plasma and gas shock; we calculate the elec-

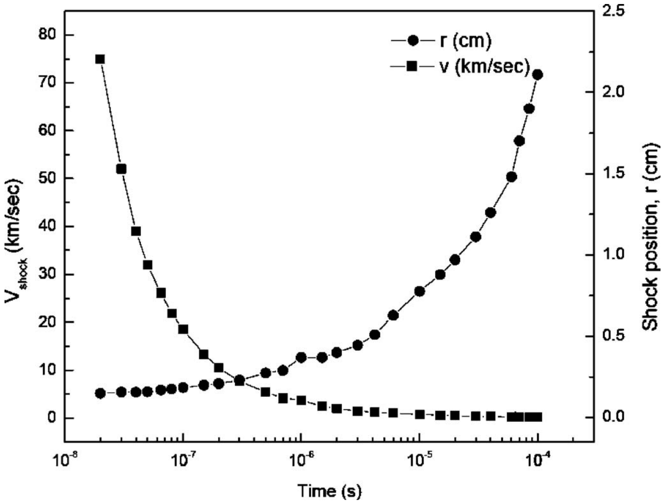


FIG. 3. Expansion of the shock (circles) and velocity (squares) of the shock front traveling against the incoming laser beam of 135 mJ.

tron temperature behind the shock front approaching values of 25 eV at $t=10$ ns and the temperature decays rapidly to 0.1 eV at 2 $\mu$s and continues to drop to 0.03 eV at 30 $\mu$s. These temperatures are comparable to those observed in longer wavelength (1.06 $\mu$m) laser focus plasma experiments.[7,20]

### D. OES: Temperature measurements

In our experiment the rotational temperature ($T_{rot}$) is determined by fitting the spectrum with SPECAIR in the range of 364–383 nm. This spectral range corresponds to the $\Delta v = -2$ vibrational sequence of $N_2 C$-$B(2+)$ band system.[13] The best-fit SPECAIR spectrum can yield rotational temperatures ($T_{rot}$) and the best-fit vibrational temperatures ($T_{vib}$) can be obtained based on the relative intensities of the (0,2), (1,3), (2,4), and (3,5) vibrational bands of the $N_2 C$-$B(2+)$ system. $T_{trans}$ is the translational neutral temperature and is often simply referred to as the neutral gas temperature in plasmas. It describes the translational velocity distributions of the $N_2$ molecules and $N_2^+$ ions in the nitrogen plasma. $T_{trans} \approx T_{rot}$ can be assumed for our atmospheric-pressure laser induced plasmas because the rotational relaxation time is fast at atmospheric pressures.[13,16] Therefore, the OES measurement of $T_{rot}$ is a reliable nonperturbing diagnostic of $T_{trans}$.

The experimental spectra measured at different times ranging from 45 ns to 100 $\mu$s are fitted with the SPECAIR code-simulated spectra as shown in Fig. 5. The best-fit SPECAIR spectrum yields rotational temperatures of $45\,350 \pm 250$ K at $t=45$ ns and the temperature decays rapidly to $2170 \pm 100$ K at 1 $\mu$s and continues to decrease to 400 K at 100 $\mu$s. The best-fit vibrational temperatures, based on the relative intensities of the (0,2), (1,3), (2,4), and (3,5) vibrational bands of the $N_2 C$-$B$ system, are $46\,000 \pm 200$ K at $t=45$ ns and decays rapidly to $2250 \pm 100$ K at 1 $\mu$s and continues to decrease to 400 K at 100 $\mu$s. For $350 < t < 650$ ns the emission spectrum is overlapped by the $O_2$ Schumann–Runge and $N_2^+(1-)$ transitions. This is because the $O_2$ Schumann–Runge and $N_2^+(1-)$ transitions dominate at temperature range from 3000 to 5000 K,[13] which our laser plasma exhibits for 300 ns $< t <$ 700 ns. During this time window the overlap between $O_2$ Schumann–Runge and other possible transitions in the shorter wavelength region makes further analysis of thermodynamics of the laser induced air plasma species impractical. As can be seen from Fig. 6, the measured temporal decays of the vibrational and rotational temperatures are to within experimental uncertainty in good agreement with one another, which signifies that the plasma is in LTE conditions for $t < \sim 2$ $\mu$s. Once the neutral shock wave gets separated from the core plasma at $t \sim 2-3$ $\mu$s, the rotational and vibrational temperatures deviate from one another and continue to decay. After $t > 2$ $\mu$s the rotational and vibrational core temperatures of the plasma are observed to be higher than the temperature just behind the shock wave. The reason for this could be due to the fact that the neutral heated shock wave expands rapidly in three dimensions; however the core plasma remains localized near the focal region and its temperature decay depends on slower diffusion processes. Therefore the rate of heat loss is much higher just behind the shock wave as compared to the core plasma.

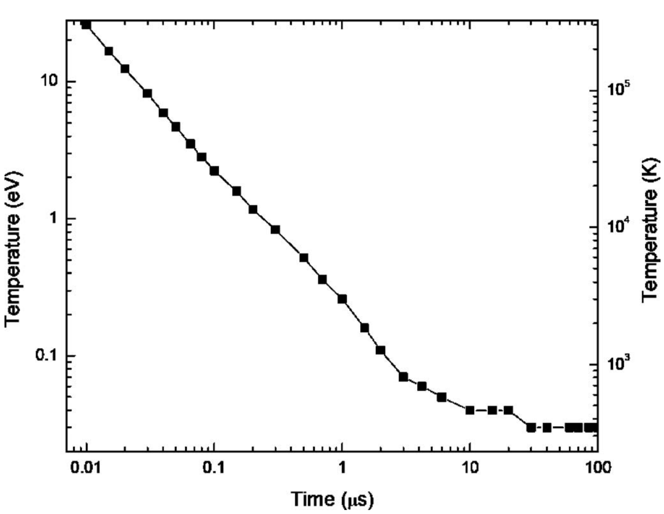


FIG. 4. Temperature decay of shock front as it expands out of the focal volume for 135 mJ laser pulse.

### E. Electron and neutral density measurements

By using probe lasers at two different wavelengths, such as red ($\lambda_R=632.8$ nm) and green ($\lambda_G=532$ nm), it is possible to distinguish between the electron and the neutral gas densities that affect the index of refraction differently. The two wavelengths, in turn, produce different phase shifts ($\phi_R$, $\phi_G$) when propagating through the plasma and neutral density core. Since our plasma is weakly ionized, two-color interferometry must be used to determine the electron density. The $O$-mode refractive index for a certain electron density increases with the laser wavelength. Electrons have by far the largest contribution to the refractive index. The high reproducibility of the discharge ($\pm 5\%$) allows us to perform measurements for certain discharge parameters independently, at each wavelength, for sequential shots.

The record of interference figures is made using the SOLIS™ software that allows one to record images with a range

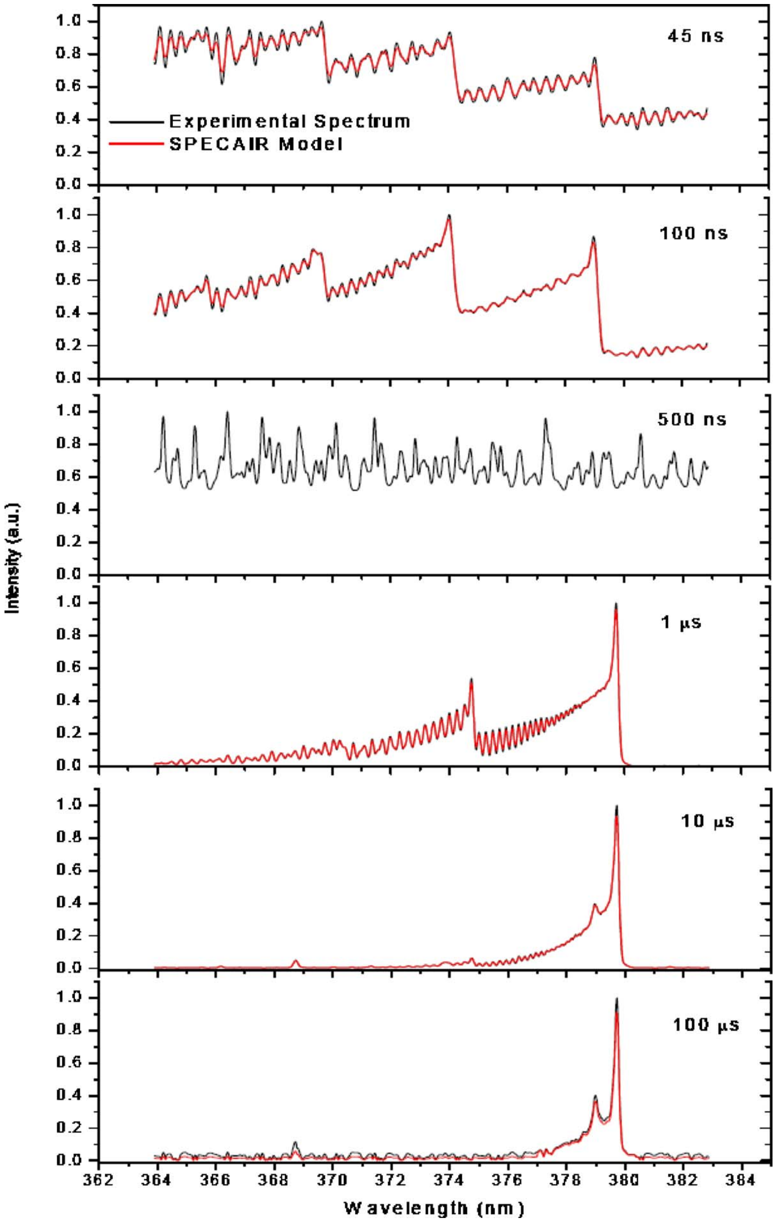


FIG. 5. (Color online) Measured $N_2$ ($C$-$B$) spectrum of the laser induced plasma; SPECAIR best-fit provides plasma temperatures.

of acquisition parameters such as delay time, gating time, and gain. In our experiment fringe interferograms are captured with 10 ns gating times. The images were captured at times $>600$ ns when plasma dimensions are large enough ($D>3$ mm) to create detectable fringe phase shift patterns. Depending on the laser energy and chamber pressure, the electron density can be measured by this technique at up to $10-80$ $\mu$s time scales, limited by the lower plasma density $n_e<10^{14}$ cm$^{-3}$ that causes measurable fringe shifts. Figure 7 presents three interference fringe figures, one without plasma and two for the plasma at 5 and 10 $\mu$s. We observe the appearance of plasma, which creates shifts in the fringes. The phase shift due to the line-integrated plasma electron number density $\phi_e$ is given by[9]

$$\varphi_e = \frac{e^2\lambda_s}{4\pi m_e \varepsilon_0 c^2}\int_0^L n_e(r)dr = r_e\lambda_s\int_0^L n_e(r)dr, \quad (4)$$

where $e$ is the electron charge, $m_e$ is the electron mass, $c$ is the light speed, $\lambda_s$ is the probe laser wavelength, $r_e$

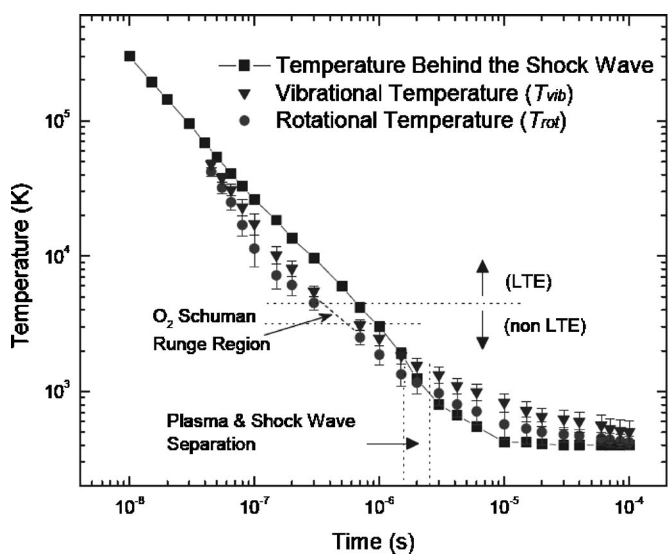


FIG. 6. Rotational and vibrational temperatures of the core plasma compared with the temperature behind the shock wave.

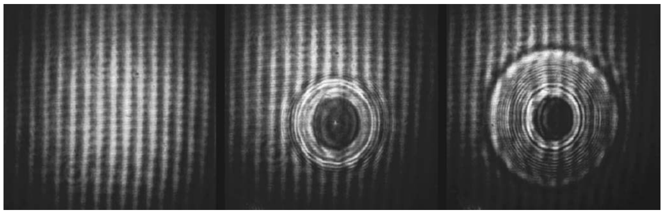

FIG. 7. Interference images for $\lambda = 532$ nm, from the left to right, without the plasma, with plasma at 5 and 10 $\mu$s.

$=e^2/(4\pi\varepsilon_0 m_e c^2)=2.818\times 10^{-13}$ cm is the classical electron radius, and $L$ corresponds to the length of the plasma crossed by the probe laser beam ($L=4$ mm). The optical length of the plasma crossed by the probe laser depends on both space and time because of the expansion of the plasma in the post-discharge stage. The value of $L$ noted is the mean value determined by the dimension of the visible plasma. Equation (4) then simplifies to

$$\phi_e = -r_e \lambda_s n_e L. \tag{5}$$

The phase shift is negative because the effective index of refraction is less than 1. The phase shift from neutrals or, more generally, from any bound electrons in neutrals or ions is related to the line-integrated neutral density $n_0 L$ by[9]

$$\phi_n = \frac{2\pi}{\lambda_s}\frac{\beta}{n_{\mathrm{atm}}} n_0 L, \tag{6}$$

where $\beta$ is the Gladstone–Dale constant, which is related to the index of refraction $\mu$ by $\beta=\mu-1$ specified at density $n_{\mathrm{atm}}$ for the given neutral species. The Gladstone–Dale constant value of 0.2257 $\mathrm{cm}^3/\mathrm{g}$ is used for air. In general the measured phase shift is the sum of electron and neutral phase shifts. By measuring phase shift at two wavelengths, the line-integrated electron and neutral densities can be calculated by combining Eqs. (5) and (6), assuming that $\beta$ is independent of wavelength,[9]

$$n_e L = \frac{1}{r_e}\frac{(\varphi_R\lambda_R - \varphi_G\lambda_G)}{(\lambda_G^2 - \lambda_R^2)}, \tag{7}$$

$$n_0 L = \frac{n_{\mathrm{atm}}}{2\pi\beta}\frac{(\phi_R\lambda_R - \phi_G\lambda_G)}{(\lambda_G/\lambda_R - \lambda_R/\lambda_G)}, \tag{8}$$

where $\phi_R(\lambda_R)$ and $\phi_G(\lambda_G)$ are the measured red and green phase shifts. We have used the Abel inversion technique[13,21] in order to measure the peak electron density at the center of the hot core plasma corresponding to a vertical fringe, as well as to measure the neutral gas density profile. It consists of transforming the profile of the mean density into a local density profile. This transformation is only possible if the mean density profile is symmetric about the center as indicated by our shadowgraphy observations. The two-color interferometry diagnostic allows one to determine the mean density integrated along a plasma chord. Assuming that the plasma has a cylindrical symmetry that is justified for our case based on shadowgraphy observations, we can determine the electron density as a function of the plasma radius. Using the Abel integration equation, the phase profile for a given fringe is written as follows:

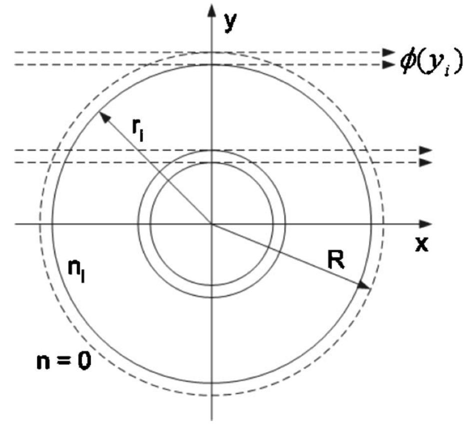


FIG. 8. Geometry of Abel inversion technique.

$$\phi(y) = \int_y^R \frac{r n_{e,0}(r)}{\sqrt{r^2 - y^2}} \times dr. \tag{9}$$

We determine the phase shift function $\phi(y)$ graphically as shown in Fig. 8. For peak electron density measurements, the few fringes at the center of the interferograms are used, and for the spatially resolved neutral gas density measurements, the entire interferogram fringes are used. Using the Abel inversion, we can obtain the local density by calculating the expression

$$n_{e,0}(r) = -\frac{1}{\pi}\int_r^R \frac{\varphi'(y)}{\sqrt{y^2 - r^2}} dy. \tag{10}$$

Figure 9 shows the results of the temporal evolution of the electron density on axis for 55 mJ absorbed and partially scattered UV laser pulse energy at 500 Torr and 1, 3, and 5 atm pressures. Figure 10 illustrates the temporal and spatial evolution of the laser heated neutral gas density for an absorbed and partially scattered laser pulse energy of 55 mJ at 760 Torr. The neutral density is given as the number of $\mathrm{molecules/cm^3}$ and there are $2.45\times 10^{19}$ $\mathrm{molecules/cm^3}$ present at STP 760 Torr air based on the ideal gas law, $pV$

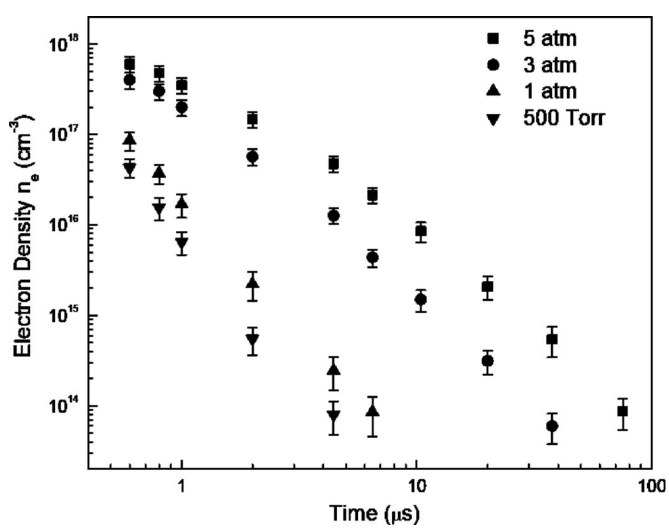


FIG. 9. Temporal electron density decay in dry air for 135 mJ laser pulse at different neutral pressures of 500 Torr and 1, 3, and 5 atm.

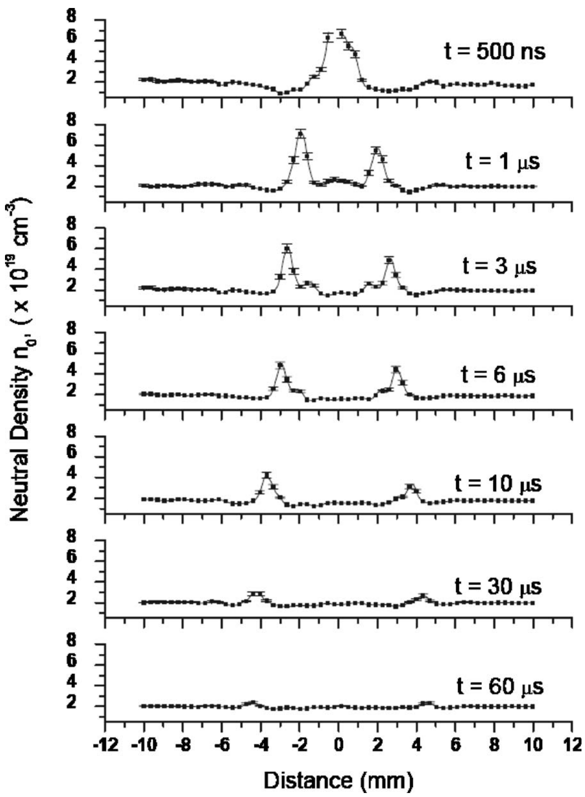


FIG. 10. Temporal and spatial evolution of the neutral density around the shock wave created by the laser focused plasma in air for 135 mJ laser pulse. A value of $2.45\times 10^{19}$molecules/cm$^3$ is used for atmospheric neutral density for air at 760 Torr.

$=Nk_BT$, in which $p$ is the pressure in Pascals, $V$ is the volume in m$^3$, $N$ is the number of molecules, and $k_B$ is the Boltzmann constant.

Both the radial expansion as well as a decrease of the shock front density can clearly be observed. The highest compression of the neutral gas density in the shock is around four times higher than the initial 1 atm gas pressure at 500 ns. The local corresponding neutral gas pressure under the LTE conditions with $T_e=5$ eV at 500 ns corresponds to 800 atm of pressure at STP room temperature conditions. The corresponding peak electron plasma pressure at 500 ns is 0.7 atm due to the lower electron density. The increase in the neutral pressure is due to the increased density from the plasma laser pulse and the increased temperature of the neutrals due to collisional coupling under the LTE conditions with the heated plasma. The neutral density in the shock eventually decays over time as the spherical shock wave expands out of the focal volume.

In Fig. 10 at time $t=500$ ns, one should expect a dip at the central peak of the increased neutral density since the shock wave has already expanded for hundreds of nanometers, but this is not resolvable due to the 0.3 mm spatial distance between the fringes of the fringing pattern. Between 500 ns and 1 $\mu$s as shown in Fig. 10, the neutral density just behind and in front of the shock wave is observed to be slightly lower than atmospheric neutral density. During this time range the fringe phase shift changes very rapidly due to the high shock wave velocity. The neutral density measurements show that high density neutrals evolve in the laser induced plasmas coincident with the density shock propagation and when the neutral density is higher in the shock wave, there is a reduced density on either side of it.

### F. Analysis of plasma density decay

We now compare the two laser plasma density decay measurements with a simplified model for the electron density decay rate continuity equation that compares different loss terms and utilizes the dominant loss terms. The measured electron number density decay rate, $dn_e/dt$, is compared with those of a detailed air plasma equilibrium analysis that incorporates the leading terms in the air plasma chemistry[19,22–25] to assess the dominant three- and two-body recombination terms as well as diffusion processes in the laser breakdown. The measured electron density and temperature data at 1 atm base pressure from the temporal density plot in Fig. 9 and the temporal temperature plot in Fig. 4, where we assume isothermal conditions in the core plasma, are used to calculate the plasma density decay rates over time when the plasma edge density and shock wave front are coincident and when the plasma size is large enough to obtain reliable density measurements, 600 ns$\leq t \leq$2 $\mu$s. The plasma density decay analysis is performed in this time window only in the core region of the plasma with a radius of $r=\pm 1$ mm, where negligible diffusion and isothermal (flat temperature) spatial profiles are assumed and indicated in other laser shock wave papers.[5,26] During this time window the measured electron density is $n_e \geq 10^{15}$ cm$^{-3}$, in which the assumption of LTE is valid.[13,21]

In the absence of an ionizing source, after the laser is turned off, the plasma decay can be described by the continuity equation[19,27]

$$\frac{dn_e}{dt} = -D_a\nabla^2 n_e - v_a n_e - \alpha_r n_e^2 - \beta_e n_e^3, \tag{11}$$

where $D_a$ stands for the ambipolar diffusion coefficient, $v_a$ is the attachment rate, $\alpha_r$ (cm$^3$/s) is the two-body (electron-ion) recombination rate coefficient,[28] and $\beta_e$ (cm$^6$/s) is the effective radiative recombination rate coefficient for three-body collisions.[23]

The term $D_a\nabla^2 n_e$ represents electron diffusion and is approximated by the term $D_a n_e/\Lambda_p^2$, where $\Lambda_p$ is the diffusion length of the plasma sphere of radius $R=2$ mm given by[19] $(1/\Lambda_p)^2=(\pi/R)^2=637$ $\mu$m. The ambipolar diffusion coefficient is given by[26] $D_a=kT_e/(m_e v_0)$, where $v_0 = n_0\sigma_0[3kT_e/m_e]^{1/2}$ is the electron-molecular effective collision frequency. The diffusion loss term at later times ($t > 600$ ns) $D_a n_e/\Lambda_p^2$ is approximately ten orders of magnitude lower than the measured plasma decay rate. The low rate of diffusion near the plasma center is verified by measurements of the radial electron density profile at incremental times (600 ns$< t <$5 $\mu$s) and higher pressures of 5 atm where the interferometer is most accurate as shown in Fig. 11. The plasma is shown to decay uniformly due to recombination in the core region of interest, i.e., $r=\pm 1$ mm, with negligible radial diffusion in the core density profile. From Figs. 4 and 9 for the 1 atm plasma at $t=600$ ns that has a maximum density of $n_e=8.6\times 10^{16}$ cm$^{-3}$ at 4600 K, the dif-

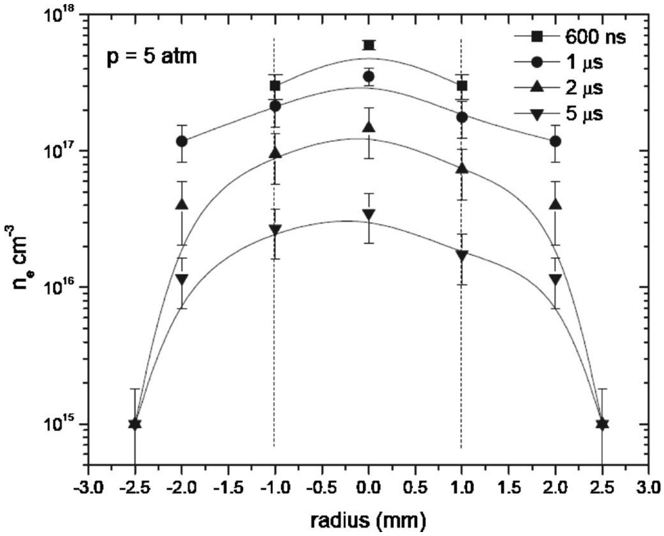


FIG. 11. Radial profile of electron density for 600 ns$<t<5$ $\mu$s at $p=5$ atm. Region of interest radius $r=\pm 1$ mm.

fusion loss term $D_a n_e/\Lambda_p^2 \sim 1.1\times 10^{13}$ cm$^{-3}$/s $\ll dn_e/dt|_{\text{expt}} \sim 2.5\times 10^{24}$ cm$^{-3}$/s and at $t=2$ $\mu$s with a plasma density of $2.2\times 10^{15}$ cm$^{-3}$ at 1300 K, the diffusion loss term $D_a n_e/\Lambda_p^2 \sim 2.7\times 10^{11}$ cm$^{-3}$/s $\ll dn_e/dt|_{\text{expt}} \sim 1\times 10^{22}$ cm$^{-3}$/s. This indicates that the diffusion loss term $D_a n_e/\Lambda_p^2 \ll dn_e/dt|_{\text{expt}}$ is small at these times and therefore it can be neglected.

The attachment of an electron to a molecule leads to the formation of a negative ion and corresponds to a decrease in the number of free electrons in the plasma. Air behaves like an electronegative gas. The attachment frequency $v_a = v_{da} + v_{3a}$ is the sum of frequencies caused by the two main attachment processes such as the dissociative attachment $v_{da}$, $O_2 + e \rightarrow O^- + O$, and the three-body attachment $v_{3a}$, $e + O_2 + M \rightarrow O_2^- + M$ $(M = O_2, N_2)$ processes.[29] The dissociative attachment frequency is defined as $v_{da} = h_a v_{en}$, where $h_a$ is the attachment efficiency, which is a weak function of electron energy, and $v_{en}$ is the electron-neutral collision frequency. The value of $h_a = 1.5\times 10^{-4}$ s$^{-1}$ given by Chan *et al.*[11] is used. The electron-neutral collision frequency is given by $v_{en} = n_0 \sigma_0 w_e$, where $\sigma_0 \approx 10^{-18}$ cm$^{-2}$ (Refs. 19 and 29) is the dissociative attachment cross section. The dissociative electron attachment frequency is obtained to be $v_{\text{da}} \approx 3\times 10^3$ s$^{-1}$. For the three-body attachment reaction, $O_2$ is used as the third body since the same reaction with $N_2$ as a third body presents much smaller cross section.[29] The three-body electron attachment rate for the attachment process $e + O_2 + O_2 \rightarrow O_2^- + O_2$ is given by[22,27,30] $2.2\times 10^{-29}[300/T_e]^{3/2}\exp[-900/T_e](\text{cm}^6/\text{s})$. At $T=4600$ K, the three-body electron attachment frequency is $v_{3a} \approx 2.2\times 10^2$ s$^{-1}$. From Figs. 4 and 9 for the 1 atm plasma at $t=600$ ns that has a maximum density of $n_e = 8.6\times 10^{16}$ cm$^{-3}$ at 4600 K, the attachment loss term $v_a n_e \sim 2.7\times 10^{20}$ cm$^{-3}$/s $\ll dn_e/dt|_{\text{expt}} \sim 2.5\times 10^{24}$ cm$^{-3}$/s and at $t=2$ $\mu$s with a plasma density of $2.2\times 10^{15}$ cm$^{-3}$ at 1300 K, the attachment loss term $v_a n_e \sim 7\times 10^{18}$ cm$^{-3}$/s $\ll dn_e/dt|_{\text{expt}} \sim 1\times 10^{22}$ cm$^{-3}$/s. This indicates that the attachment loss term $v_a n_e \ll dn_e/dt|_{\text{expt}}$ is small at these times and therefore is neglected. Thus the continuity equation [Eq. (11)] takes the form

$$\frac{dn_e}{dt} = -\alpha_r n_e^2 - \beta_e n_e^3. \tag{12}$$

Another loss process affecting the electron density is the charged particle recombination—electrons with positive ions or negative ions with positive ions. For electron-ion recombination, there are two- and three-body recombination processes. The two-body electron-ion recombination rate $\alpha_r$ is a sum of dissociative $\alpha_{dr}$ and radiative $\alpha_{rr}$ recombination rates. The dissociative recombination mechanism $M_2^+ + e \rightarrow M + M^*$ $(M = O_2, N_2)$ is the fastest mechanism of bulk recombination in weakly ionized plasma.[19] In the $M^*$ notation, the asterisk indicates an electronically excited state, in this case, the $(^1S)$ state. The electron dissociative recombination coefficients $\alpha_{dr}$ for $N_2^+$ and $O_2^+$ as a function of electron temperature $T_e$ are given by[22,30,31]

$$\alpha_{dr(1)} = 2.035\times 10^{-6} T_e^{-0.39}[e^- - N_2^+]\text{cm}^3/\text{s}, \tag{13}$$

$$\alpha_{dr(2)} = 1.138\times 10^{-5} T_e^{-0.7}[e^- - O_2^+]\text{cm}^3/\text{s}. \tag{14}$$

The total electron-ion dissociative recombination coefficient for air, considering the ratios of $N_2$ and $O_2$ ($N_2$: 79%; $O_2$: 21%) in air, is $\alpha_{\text{dr}} = 0.79\alpha_{\text{dr}(1)} + 0.21\alpha_{\text{dr}(2)}$. The cross sections of the radiative recombination process $M^+ + e \rightarrow M + hv$ are very small ($\sigma_{\text{rr}} \sim 10^{-21}$ cm$^2$).[19] The radiative recombination coefficient $\alpha_{\text{rr}}$ is also correspondingly small,[19,23]

$$\alpha_{\text{rr}} = \langle v\sigma_c\rangle \approx 2.7\times 10^{-13}(T_e)^{-3/4}\ \text{cm}^3/\text{s}. \tag{15}$$

The total two-body recombination coefficient $\alpha_r$ $(\alpha_{\text{dr}} + \alpha_{\text{rr}})$ is calculated using the above rate equations and compared with the recombination coefficient calculated from the measured electron densities $n_{e1}$ and $n_{e2}$ at two closely spaced measurement times $t_1$ and $t_2$, respectively, using the expression[28]

$$\alpha_r = \frac{\left(\frac{1}{n_{e2}} - \frac{1}{n_{e1}}\right)}{(t_2 - t_1)}. \tag{16}$$

Using the 1 atm data from the temporal density plot in Fig. 9, the two-body recombination coefficient $\alpha_r$ is obtained and increases from $7.6\times 10^{-11}$ cm$^3$/s at 600 ns to $1.5\times 10^{-9}$ cm$^3$/s at 2 $\mu$s. From Figs. 4 and 9 for the 1 atm plasma at $t=600$ ns that has a maximum density of $n_e = 8.6\times 10^{16}$ cm$^{-3}$ at 4600 K, the two-body recombination loss term $\alpha_r n_e^2 \sim 5.6\times 10^{23}$ cm$^{-3}$/s $\ll dn_e/dt|_{\text{expt}} \sim 2.5\times 10^{24}$ cm$^{-3}$/s and at $t=2$ $\mu$s with a plasma density of $2.2\times 10^{15}$ cm$^{-3}$ at 1300 K, the two-body recombination loss term $\alpha_r n_e^2 \sim 7.3\times 10^{21}$ cm$^{-3}$/s $\approx dn_e/dt|_{\text{expt}} \sim 1\times 10^{22}$ cm$^{-3}$/s. The two-body recombination loss term $\alpha_r n_e^2(\text{cm}^{-3}/\text{s})$ is plotted (dots) in Fig. 12. The solid line shows the measured density decay rate $(dn_e/dt|_{\text{expt}})$. It is observed that the two-body recombination rate is dominant for times $t \geq 1.05$ $\mu$s. At early times, i.e., 600 ns$<t<1.05$ $\mu$s, the two-body recombination rate is smaller and the three-body recombination process dominates.

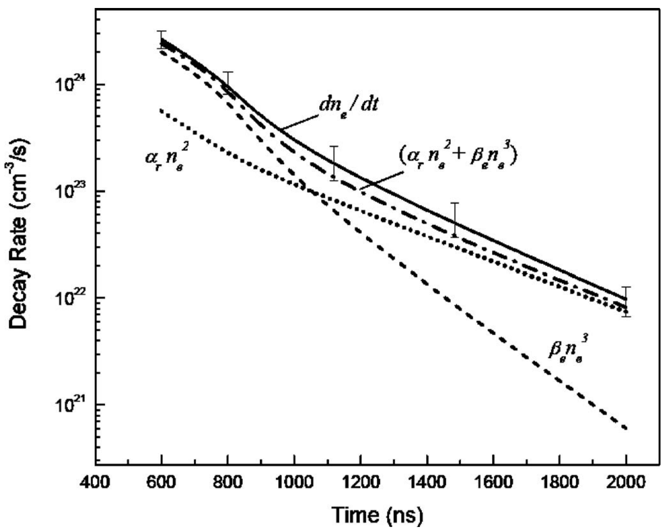


FIG. 12. Plasma decay rate and recombination loss rate ($p$=760 Torr).

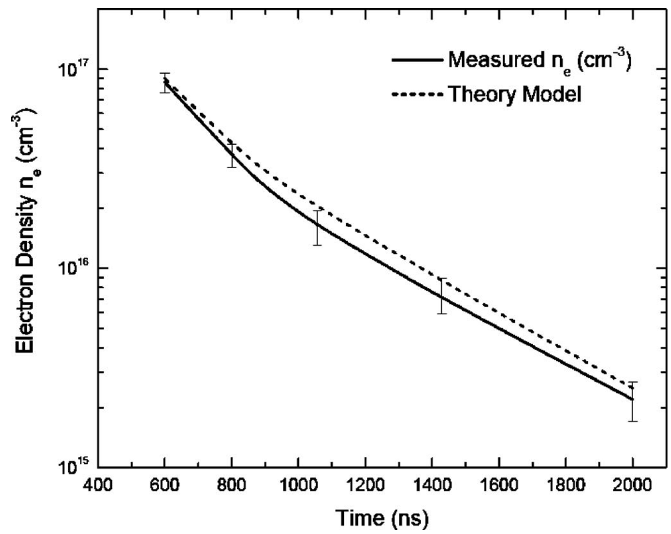


FIG. 13. Measured electron density decay compared with approximate theoretical plasma decay model.

The three-body recombination process follows the scheme $A^+ + e + e \rightarrow A + e$; it is observed to be the main process for high-density low-temperature equilibrium plasmas.[19,28] In three-body collisions, electrons are captured by ions forming excited atoms with a binding energy of order $kT$. Subsequent electron impacts deactivate the excited atom gradually and fall to the ground state by a radiative transition. The effective three-body recombination rate coefficient $\beta_e(\mathrm{cm}^6/\mathrm{s})$ is a function of electron temperature. It is given by[23,27]

$$\beta_e = 1.32 \times 10^{-27} (T_e/10^4)^{-4.66} \mathrm{cm}^6/\mathrm{s}. \tag{17}$$

The three-body recombination rate $(\beta_e n_e^3)$ is plotted (dashes) in Fig. 12. At $t$=600 ns the three-body recombination loss term $\beta_e n_e^3 \sim 1.97 \times 10^{24}\ \mathrm{cm}^{-3}/\mathrm{s} \approx dn_e/\,dt|_{\mathrm{expt}} \sim 2.5 \times 10^{24}\ \mathrm{cm}^{-3}/\mathrm{s}$ and at $t$=2 $\mu$s the three-body recombination loss term $\beta_e n_e^3 \sim 7 \times 10^{20}\ \mathrm{cm}^{-3}/\mathrm{s} \ll dn_e/\,dt|_{\mathrm{expt}} \sim 1 \times 10^{22}\ \mathrm{cm}^{-3}/\mathrm{s}$. The values we obtain are comparable to published collisional three-body recombination rates for singly ionized plasmas.[8,28] The three-body loss rate $\beta_e n_e^3$ is dominant $(\beta_e n_e^3 \sim dn_e/dt)$ when $n_e > 2 \times 10^{16}\ \mathrm{cm}^{-3}$ for times 600 ns$<t<$1050 ns and the electron temperature is 0.25 eV. For times $t>$1050 ns $(n_e < 10^{16}/\mathrm{cm}^3)$ the two-body recombination processes dominate the three-body recombination processes with different recombination rates as will be discussed earlier.

For 600 ns$<t<$2000 ns, the sum of the major loss terms including the two- and the three-body recombination process, as shown (dash-dot-dash) in Fig. 12, fits close to the measured electron density decay rate. Figure 13 shows the actual electron density decay (solid line) compared with the approximate theoretical plasma decay (dashes), which is the integral of Eq. (19). It is observed that the electron density based on the theoretical model decays at a slower rate compared to the measured electron density. The reason for the slower decay is possibly due to the fact that only two major loss terms incorporating two- and three-body recombination processes are considered in our theoretical model. Although less dominant, there are numerous other complex reaction processes involved in air plasma chemistry and their incorporation could further close the difference between our measured data and the theoretical model.

## IV. SUMMARY

The measurements of laser induced breakdown plasma properties for air using 193 nm, 200 mJ, 20 ns, 10 MW excimer laser radiation for pressures ranging from 40 Torr to 5 atm where multiphoton as well as collisional cascade processes are significant has been carried out. For 135$\pm$5 mJ laser incident energy, an average of 80$\pm$5 mJ energy was measured to be transmitted through the plasma, which is 60% of the incident energy. Therefore approximately 55 mJ (40% of incident energy) of the excimer laser pulse energy was absorbed at 760 Torr by the plasma at the focal region. The energies absorbed by the plasma, at different pressures such as 500 Torr, 3 atm, and 5 atm, are measured to be 48, 64, and 76 mJ, respectively, which correspond to 35%, 47%, and 56% of the incident energy, as expected with the increased absorption with pressure.

The shadowgraphy diagnostics were performed to analyze the spatial and temporal evolution of the laser induced plasma. Using this diagnostic, the plasma volume, shock wave velocities, and hot core air pressures were also measured. An average shock wave velocity of 47 km/s was measured from the expanding plasma and the laser heated neutral shock wave. Based on the measured velocities of the plasma and gas shock, we have calculated the electron temperature behind the shock front approaching values of 25 eV at $t$=10 ns, and the temperature decays rapidly to 0.1 eV at 2 $\mu$s and continues to drop to 0.03 eV at 30 $\mu$s.

The two-color laser interferometry diagnostics were implemented and measured both the spatial and temporally resolved electron and neutral number densities. Based on the measurements it is observed that the highest compression of the neutral gas density in the shock is around four times higher than the initial 1 atm gas pressure at 500 ns. UV laser focus provides Poynting flux intensities in the $>1$ TW/cm$^2$

range that produce neutral density shock wave pressures as high as 800 atm at STP under LTE conditions with $T_e = 5$ eV at 500 ns, and the corresponding peak electron plasma pressure at 500 ns is 0.7 atm due to the lower electron density. The electron densities were measured for pressures of 500 Torr, 1 atm, 3 atm, and 5 atm. The electron density measured at 600 ns increased from $8.6 \times 10^{16} \text{cm}^{-3}$ at 1 atm to $6 \times 10^{17}$ $\text{cm}^{-3}$ at 5 atm. At 760 Torr gas pressure the plasma electron density was observed to decay from $8.6 \times 10^{16}$ $\text{cm}^{-3}$ at 600 ns to $0.9 \times 10^{14}$ $\text{cm}^{-3}$ at 6.5 $\mu$s.

The two laser plasma density decay measurements are compared with a simplified model for the electron density decay rate continuity equation that compared different terms and utilizes the dominant three- and two-body recombination terms for 600 ns$<t<$2 $\mu$s. The measured electron number density decay rate, $dn_e/dt$, is compared with those of a detailed air plasma equilibrium analysis that incorporated the leading terms in the air plasma chemistry literature and assessed the dominant three- and two-body recombination terms as well as diffusion processes in the laser breakdown. It was shown that the diffusion and attachment losses are negligible compared to the recombination losses. At early times, i.e., 600 ns$<t<$1050 ns, the two-body recombination loss term is shown to be smaller than the three-body recombination loss term. However, it is observed that the two-body recombination rate is dominant for times $t \geq 1050$ ns. The sum of the calculated two- and three-body recombination loss model provides results in a slightly lower rate than the measured plasma decay results and, therefore, these two loss processes are the dominant terms during the observation period. The close agreement between the measured density decay rate and the modeled decay rate shows consistency and supports the measured values as well as illustrates the dominant influence of the two recombination terms we have considered.

OES measurements are used for the temporal measurements of rotational and vibrational temperatures of the core plasma. The temperatures are observed to be in close agreement with the temperature behind the shock wave when the plasma is in LTE and when the shock wave closely encompasses the plasma volume. The plasma was observed to be in LTE for $t < \sim 2$ $\mu$s, during which the rotational and vibrational temperatures of the core plasma converge together. After $t > 2$ $\mu$s the rotational and vibrational temperatures of the plasma are observed to be higher than the temperature behind the shock wave. Due to the separation of neutral shock wave from the core plasma after $t \sim 2$ $\mu$s, the rotational and vibrational temperatures deviate from one another. For $t > 2$ $\mu$s the neutral heated shock wave continues to expand spherically in three dimensions; however the core plasma remains localized near the laser focal region.

## ACKNOWLEDGMENTS

The authors thank C. Mark Denning for assistance. This research is supported in part by Air Force of Scientific Research (AFOSR) Grant No. FA9550-06-1-0172 and DURIP equipment Grant No. FA9550-06-1-0285.

[1] C. Phipps, *Laser Ablation and its Applications*, 1st ed. (Springer, New York, 2006).
[2] J. Stricker and J. G. Parker, J. Appl. Phys. **53**, 851 (1982).
[3] C. A. David, *Lasers-Induced Plasmas and Applications* (CRC, Boca Raton, 1989).
[4] H. Yan, R. Adelgren, M. Boguszko, G. Elliott, and D. Knight, AIAA J. **41**, 10 (2003).
[5] I. P. Shkarofsky, RCA Rev. **35**, 48 (1974).
[6] N. Glumac, G. Elliot, and M. Boguszko, AIAA J. **43**, 1984 (2005).
[7] M. Villagran-Muniz, H. Sobral, and E. Camps, IEEE Trans. Plasma Sci. **29**, 613 (2001).
[8] Y. B. Zeldovich and Y. P. Raizer, *Physics of Shock Waves and High-Temperature Hydrodynamic Phenomena* (Academic, New York, 1966).
[9] B. V. Weber and S. F. Fulghum, Rev. Sci. Instrum. **68**, 1227 (1997).
[10] C. O. Laux, *Radiation and Nonequilibrium Collisional-Radiative Models*, von Karman Institute Lecture Series 2002–07 (Rhode-Saint-Genèse, Belgium, 2002).
[11] C. H. Chan, C. D. Moody, and W. B. McKnight, J. Appl. Phys. **44**, 1179 (1973).
[12] K. H. Becker, U. Kogelschatz, K. H. Schoenbach, and R. J. Barke, *Non-Equilibrium Air Plasmas at Atmospheric Pressure* (Institute of Physics, Bristol, 2005).
[13] C. O. Laux, T. G. Spence, C. H. Kruger, and R. N. Zare, Plasma Sources Sci. Technol. **12**, 125 (2003).
[14] C. O. Laux, Ph.D. thesis, Stanford University, 1993.
[15] C. Park, *User's Manual Technical Memorandum* (NASA-Ames Research Center, Moffett Field, CA, 1985).
[16] D. Staack, B. Farouk, A. F. Gutsol, and A. A. Fridman, Plasma Sources Sci. Technol. **15**, 818 (2006).
[17] H. R. Griem, *Principles of Plasma Spectroscopy* (Cambridge University Press, Cambridge, 1997).
[18] H. R. Griem, *Plasma Spectroscopy* (McGraw-Hill, New York, 1964).
[19] Y. P. Raizer, *Gas Discharge Physics* (Springer-Verlag, Berlin, 1991).
[20] M. Villagran-Muniz, H. Sobral, and R. Navarro-Gonzalez, Meas. Sci. Technol. **14**, 614 (2003).
[21] S. Yalcin, D. R. Crosley, G. P. Smith, and G. W. Faris, Appl. Phys. B: Lasers Opt. **68**, 121 (1999).
[22] A. Takahashi and K. Nishijima, Jpn. J. Appl. Phys., Part 1 **37**, 313 (1998).
[23] A. Bourdon, Y. Teresiak, and P. Vervisch, Phys. Rev. E **57**, 4684 (1998).
[24] D. R. Bates, J. Phys. B **13**, 2587 (1980).
[25] M. Capitelli, C. M. Ferreira, B. F. Gordiets, and A. I. Osipove, *Plasma Kinetics in Atmospheric Gases* (Springer-Verlag, Berlin, 2000).
[26] S. Soubacq, P. Pignolet, E. Schall, and J. Batina, J. Phys. D **37**, 2686 (2004).
[27] G. Bekefi, *Principles of Laser Plasmas* (Wiley, New York, 1976).
[28] K. Akhtar, J. E. Scharer, S. M. Tysk, and C. M. Denning, IEEE Trans. Plasma Sci. **32**, 813 (2004).
[29] N. A. Dyatko, M. Capitelli, R. Celiberto, and A. P. Napartovich, Chem. Phys. Lett. **263**, 305 (1996).
[30] M. Miki and A. Wada, J. Appl. Phys. **80**, 3208 (1996).
[31] X. M. Zhao, J. Diels, C. Y. Wang, and J. M. Elizondo, IEEE J. Quantum Electron. **31**, 599 (1995).